ACS OMEGA

Open Access

http://pubs.acs.org/journal/acsodf

Article

Understanding the Capacitive and Diffusion-Controlled Behavior of Electrophoretically Deposited V_2CT_x on Carbon Yarn as a Potential Anode for Asymmetric Devices

Amjid Rafique,* Usman Naeem, Ana Marques, Isabel Ferreira, Syed Rizwan, and Ana Catarina Baptista*

Cite This: *ACS Omega* 2025, 10, 7621−7634

Read Online

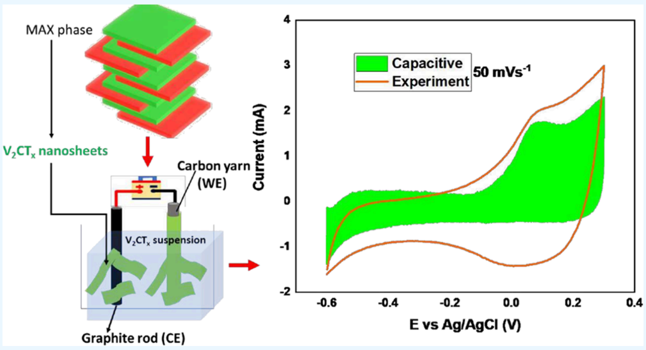

ABSTRACT: Recently, a novel class of emerging 2D materials identified as MXene have been revolutionizing the fabrication and development of flexible energy storage systems, i.e., batteries and supercapacitors. Herein, the focus is on the remarkable capacitive performance of V_2CT_x MXene-based flexible electrodes so far poorly explored. However, research was focused on $Ti_3C_2T_x$ and its applications in the energy field, although more than 100 other members of this group have already been reported. Some of these MXenes are emerging as potential candidates for energy applications with promising results such as Ti_2C and Mo_2C in aqueous electrolytes, but many others remain to be explored. The paper detailed a comprehensive study of the electrophoretic deposition of V_2CT_x on carbon yarn wires and the evaluation of their electrochemical behavior (capacitive and diffusive) in three electrolytes at different pH values: acidic, basic, and neutral pH to investigate the correct potential window for this material in energy applications. The devices exhibited specific capacitances of 248, 177, and 89 F g^{-1} for EPD10, EPD20, and EPD30, respectively. The synthesized and deposited MXene nanoparticles were analyzed by XRD, Raman, and SEM for phase identification, chemical structure identification, and morphological analysis, respectively. The synthesized material showed good electrochemical performance in terms of cyclic stability after 3000 cycles with >90% capacitance retention.

1. INTRODUCTION

Extensive technological advancement in communication techniques (e.g., 5G), robotics, and the Internet of Things (IoT) is likely to drive the fourth industrial transformation.[1−3] IoT connects different electronic gadgets, groups, data, and processes, providing an interface to which they communicate effortlessly. This has helped to improve various processes by gathering and disseminating large data in real time in more quantifiable and measurable ways.[4] Miniaturized sensor networks are mandatorily surrounded by IoT networks for health, environment, or industry monitoring, transportation, and flexible wearable electronics. For all these devices to work around the clock for real-time data access, a continuous power supply is required, which is still a challenge.[5] Supercapacitors (SCs) are promising energy storage devices owing to their extended cycles, fast charge/discharge, high power delivery, clean and environmentally friendly devices.[6] Electrodes are the key building block of SC devices, and their performance greatly influences device functionality.[7,8]

The properties of the active materials used for electrode fabrication, particularly at the nanoscale, and their stability affect the efficiency and performance of the device in real-time applications.[9] At the nanoscale, the structure of materials has been classified into four categories based on their quantum confinement 0D,[9] 1D,[10] 2D,[11] and 3D.[12] "2D" carbon and its derivatives comprising reduced graphene oxide (rGO), graphene, CNTs, and CFs have been used as active materials for SC electrodes owing to their unique structural properties and cost-effectiveness.[13] Carbon-based composites with transition metal oxides have also improved the capacitance of active materials and SCs. Ruoff et al.[14] described the synthesis of rGO by chemical modification of graphene and used it as an electrode material for SC electrodes and reported gravimetric capacitances of 135 and 99 F g^{-1}. Similarly, Rao et al. synthesized graphene using three different techniques and compared it with lab-scale synthesized single-wall carbon nanotubes (SWCNTs) and multiwall carbon nanotubes

Received: June 29, 2024
Revised: December 3, 2024
Accepted: December 20, 2024
Published: February 19, 2025

ACS Publications

https://doi.org/10.1021/acsomega.4c06035

(MWCNTs).[15] Although these carbon-based materials showed high electrochemical performance, they suffer from stability and low energy density due to carbon chemistry. These materials need to be composite with other transition metal oxide to fabricate high energy storage devices. Therefore, the exploration and synthesis of new active materials are imperative for the fabrication and use of SC devices for high-performance applications.[16,17]

The 2D transition metal carbides/nitrides are generally represented by $M_{n+1}AX_n$ or $M_{n+1}X_nT_x$ (MC or MCT_x can be used interchangeably) where M represents the transition metal, A represents carbide/nitrides, and T_x or X_n represents the terminal functional group such as OH^-, O^-, and F^-, which are responsible for the hydrophilic nature of MXene.[18,19] Vanadium carbide MXene (V_2CT_x) has shown excellent electrical conductive properties and cyclic stability in acidic, basic, and neutral pH as well as metal oxide/hydroxide surfaces with tunable attributes.[20] The overall properties reveal the potential for exploitation in high-performance pseudocapacitors and other energy storage devices. Fabrication of binder-free electrodes helps to achieve high gravimetric capacitance and extended life of MXene-based SCs, especially of flexible electronics.[21] This has been successfully achieved through thin film deposition of V_2CT_x and fabrication of binder-free electrodes with enhanced availability of interlayer spaces operating in amalgamated LiF and concentrated HCl solutions.[22] However, owing to interlayer binding in 2D materials,[23] the permanent stacking of layers may constantly occur throughout the electrode fabrication and active material loading process, resulting in MXene surface and functional groups.[24] The increase of interfacial resistance among MXene frontiers can foster restricted electron transfer under high currents and limit the capacitance of SCs.[24] MXene nanosheets are typically prepared as active material or as a composite active material for electrode fabrication using dispersion processes that result in self-stacking, or aggregation hindering electrolyte access to active sites and resulting in poor electrochemical performance.[25] Additives such as conductive materials and binders are added to the slurry to increase the adhesion of the active material to the substrate, but they inevitably curtail the exposed surface area of the electrode materials, increase the internal resistance, and thus compromise the potential electrochemical performance of electrodes.[26] Therefore, suitable deposition techniques are required to fabricate binder-free electrodes for SCs.

Electrophoretic deposition (EPD) is one of the deposition techniques that offer the fabrication of binder-free loading of the active material as a result of the potential applied to a stable colloidal suspension between two electrodes and resulting in direct deposition of varied morphologies of nanostructures of active materials on diverse flexible substrates.[27] Compared to other deposition techniques of fabrication such as vacuum filtration,[28] chemical vapor deposition,[29] electrochemical deposition, and dropping mild baking approach.[30] EPD offers advantages such as simple experimental setup, high deposition rate, excellent uniformity of the deposited film, the possibility of scalability, remarkable control over film thickness, and binder-free deposition,[31,32] which is the most important apprehension as far as large-scale production is concerned. Considering the above advantages, EPD is well suited to fabricating flexible electrodes on various substrates with excellent electrochemical performance for SCs. However, reports on the fabrication of V_2CT_x/CY electrodes by EPD are limited but carbon yarns electrophoretically coated with V_2CT_x for flexible SC applications do not exist to the best of our knowledge.

Among the extended groups of 2D MXene materials, V_2CT_x is the most important as vanadium surface layers could potentially exhibit pseudocapacitive behavior. Previously, V_2CT_x has been shown to exhibit an ion intercalation charge storage mechanism, when used as an active material in Na-ion and Li-ion batteries.[33,34] Here, a binder-free electrode based on V_2CT_x is fabricated via EPD for a flexible wire SC application. Initially, the deposition was performed at a fixed potential of 20 V for 10, 20, and 30 min, and the electrochemical performance of fabricated electrodes was compared. This study presents a deep electrochemical analysis of the charge storage behavior of V_2CT_x/CY in three different electrolytes at different pH levels, namely, H_2SO_4 (acidic), KOH (basic), and Na_2SO_4(neutral).

2. MATERIALS AND EXPERIMENT

2.1. Materials.

The materials used for the etching process included hydrofluoric acid (50% in H_2O ≥99.99%, Sigma-Aldrich), aluminum powders (99.999% Sigma-Aldrich), vanadium purity 99.7%, NaOH ≥98%, pellets (anhydrous, Sigma-Aldrich), HNO_3 (65% Sigma-Aldrich), KOH ≥99.99% (Sigma-Aldrich), H_2SO_4 ≥98% (Sigma-Aldrich), and Na_2SO_4 ≥99.0%. Commercial carbon yarn (Tenax-E HTA40 E13 3K 200tex) was used as a flexible current collector. All of the chemicals are of analytical nature and used as received without any further treatment.

The MAX phase was synthesized by blending metallic powders of V and Al with carbon in a stoichiometric ratio of V:Al:C = 2:1:1. The powders were homogenized in a PM100 (Retsch) planetary ball milling machine at 300 rpm using a zirconia ball at a weight ratio of 1:6 for 16 h. After every hour of milling, the system was paused for 15 min to avoid overheating. The homogeneously mixed powders were then transferred to an alumina crucible and covered with a graphite sheet for sintering. The powders were shifted to a tube furnace and sintered at 1723 K for 4 h at a ramp rate of 3.5 K/min under an argon environment. The synthesized MAX was drilled with a mill bit and sieved through a 400 mesh.

The wet chemical etching technique was used for the synthesis of V_2CT_x. At approximately 20 min, 4 g of synthesized V2AlC MAX phase was gradually added in a 10 mL solution of 50% HF solution in a Teflon beaker and left on stirring at 400 rpm for 92 h. The obtained mixture was then repeatedly cleaned with deionized (DI) water using a centrifuge at 4200 rpm for 5 min until the neutral pH of the solution was achieved. Finally, the neutralized powder was vacuum filtered to obtain V_2CT_x MXene, which was vacuum oven-dried at 35 °C for 12 h.

2.2. Activation of Carbon Yarn.

Before the EPD of 2D MXene on carbon yarn (CY), the CY wires were first activated by using a chemical method. The CY wires were washed in an acetone solution at 60 °C for 4 h to desize and to remove organic contaminants from CY surfaces. After repeatedly washing with DI water, the CY wires were dried at 100 °C for 8 h. The CY wires oxidized at 450 °C for 30 min at a rate of 2 °C/min. To improve and recover surface activation,[35] the oxidized CY wires were immersed in HNO_3 at 50 °C for 16 h. The treated CY wires were then cleaned several times with DI water until 7 pH of the solution was achieved and dried in a vacuum oven at 100 °C for 2 h.

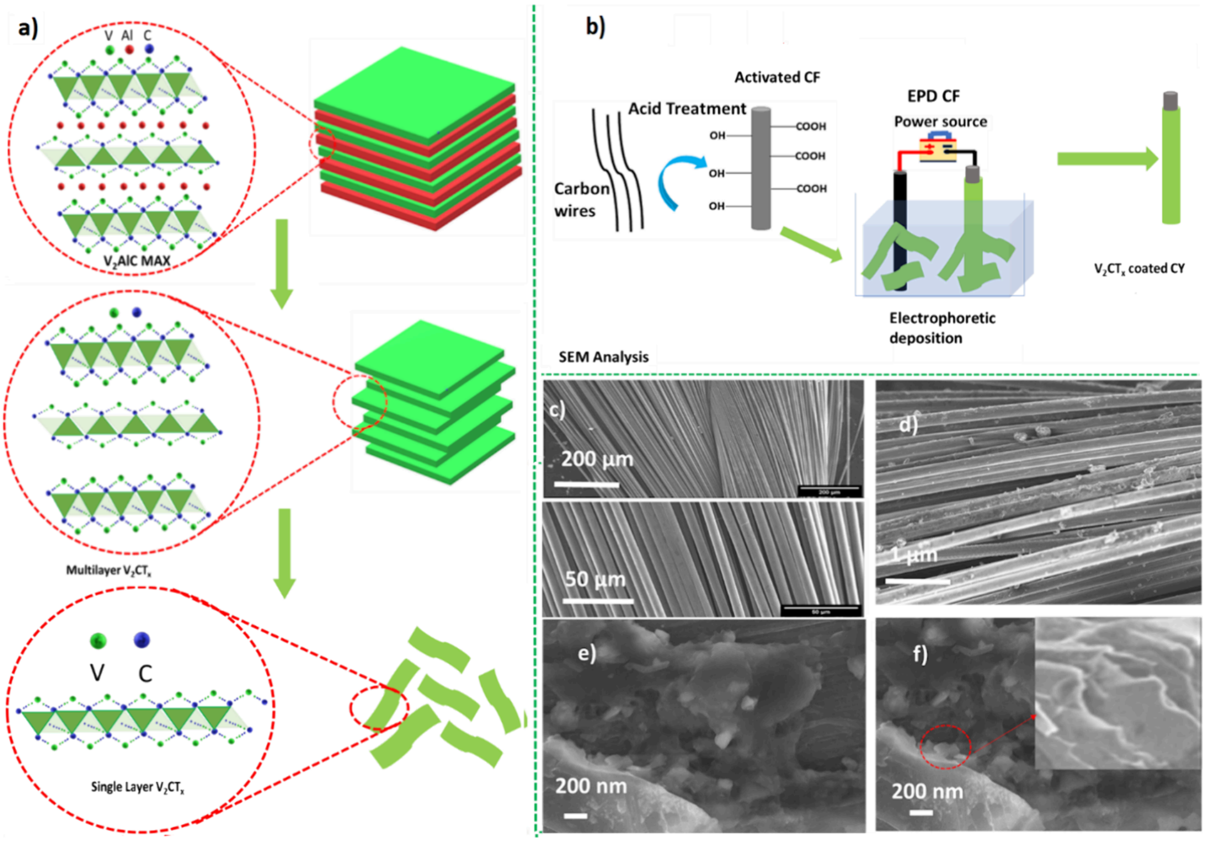

Figure 1. (a) Graphical illustration of the synthesis of MXene (V_2CT_x), (b) electrophoretic deposition of 2D MXene (V_2CT_x) carbon yarn, (c) SEM image of pristine carbon yarn, (d) SEM image of V_2CT_x-coated carbon yarn, (e, f) higher-magnification images of V_2CT_x nanosheets.

2.3. Electrophoretic Deposition of V_2CT_x MXene Nanoparticles on CY.

First, V_2CT_x nanoparticles were synthesized, and a suspension was prepared to be used as chemical bath for electrodeposition. An ultralow-concentration 100 mL suspension of MXene was prepared using 0.125 mg/mL of V_2CT_x in DI water to facilitate agglomeration of MXene nanoparticles. After the synthesis completed, CY was activated and used as the working electrode and graphite rod as the cathode. The electrophoretic deposition of V_2CT_x on CY was done using a modified process reported elsewhere.[36] The prepared electrodes were termed MXene−CY composite electrodes. A small magnetic stirrer (bar) was attached at the bottom of the CY wire to keep the wire straight and prevent it from bending, which helps in the uniform deposition of nanoparticles. During the EPD process, the distance between the anode and cathode electrodes was kept 2 cm apart, and NaOH was dropwise added to the slurry to maintain the pH at 10 for a stable and homogeneous MXene precursor. The EPD was performed at a low potential of 20 V for different durations such as 10, 20, and 30 min. Continuous stirring was performed to reduce the bubble formation due to water electrolysis, which contributed to the homogeneous deposition of the V_2CT_x layer on the CY wire.

2.4. Morphological and Electrochemical Characterization.

The morphology of the samples was analyzed by optical microscopy (Leica DMi8) and scanning electron microscopy (SEM) (Carl Zeiss AURIGA CrossBeam SEM-FIB). The crystalline structure of the electrode materials was examined using a PANalytical X'Pert Pro X-ray diffractometer in Bragg/Brentano configuration with Cu (Kα) as an X-ray source. The chemical composition of the composite electrode and the active material was investigated by confocal Raman spectroscopy (WITec alpha300 RAS) using a laser source with an excitation wavelength of 532 nm. The V_2CT_x powder and V_2CT_x-coated yarn spectra were acquired with the laser set to 2 and 5 mW, respectively, and the corresponding times were 7.5 and 5 min.

The electrochemical performance was evaluated by cyclic voltammetry (CV), galvanostatic charge/discharge cycling (GCD) measurements, and electrochemical impedance spectroscopy (EIS) in the three-electrode configuration using a Gamry 1010 potentiostat/galvanostate workstation.

2.5. Capacitance Calculations.

The three-electrode configuration was used to investigate the electrochemical performance using CV, GCD, and EIS measurements. CV curves were recorded in different potential window ranges at different scan rates (5 to 500 mV s^{-1}). The capacitance was calculated using eq 1 from the CV plots:[37]

$$C_{\text{cell}} = \frac{Q}{2V} = \frac{1}{2V\nu}\int_{\nu-}^{\nu+} i(V)\mathrm{d}V \tag{1}$$

where C_{cell} represents cell capacitance, i is the current, ν is the scan rate, and V denotes the potential window. The gravimetric capacitance was determined using eq 2, where the mass of an entire electrode was used for the calculation:

$$C_{\text{SP}} = \frac{C_{\text{cell}}}{m} \tag{2}$$

where m is the mass of the loaded active material.

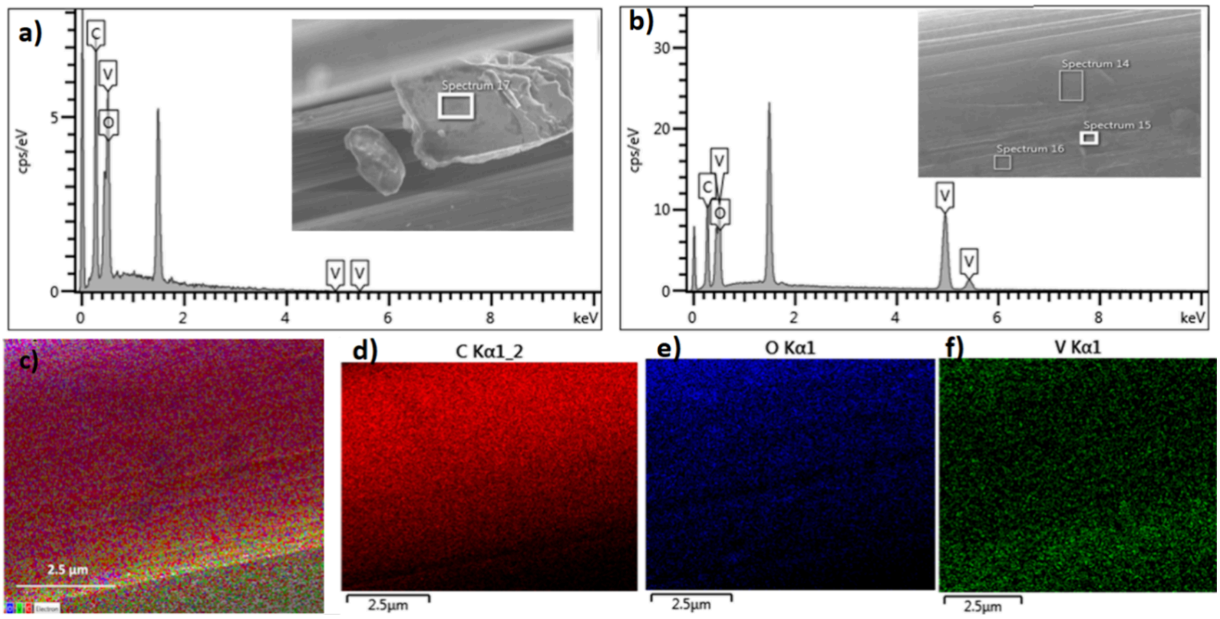

Figure 2. (a, b) EDX spectra of MXene (V_2CT_x/CY) coated on the carbon yarn. (c−f) EDX mapping of electrophoretically depositED 2D V_2CT_x/CY.

3. RESULTS AND DISCUSSION

Figure 1a,b shows two different processes. Figure 1a shows the synthesis process of V_2CT_x nanosheets through HF selective etching, while Figure 1b shows the EPD of nanosheets on the CY. Figure 1a demonstrates the typical layer formation of the V_2AlC MAX phase and the corresponding HF etching technique used to synthesize V_2CT_x. The reactive Al layers bridge and connect two vanadium sublayers with carbon atoms at octahedral interstitial sites. During the etching process in HF solution, the reactive Al is selectively etched away, leaving a periodic 2D interlayer of V_2CT_x, as shown in Figure 1a. The Al layer is removed from the MAX phase, which is indicated in Figure 1a (left side) by offset of the Al atom. The distinctive 2D layered structures can enhance electron transport by shortening the diffusion path. This offers increased interactions of electrolyte ions with active sites of the electrode material, hence improving the active material's pseudocapacitive performance. The flexible electrode was fabricated by the EPD method, and the preparation route of fabrication is shown in Figure 1b. The fabricated electrodes were referred to as V_2CT_x/CY composite electrodes. The working electrode (activated CY) was connected to the positive terminal, and the graphite rod used as the counter electrode was connected to the negative terminal. Before deposition, the oxidation process was performed in ambient air to oxidize the wax or finishes applied to the CY and other organic pollutants that were not removed during ethanol/acetone washing. Subsequently, the oxidized wires were treated with an HNO_3 solution to restore their surface activation and conductivity. These activated CY wires were used as working electrodes for the EPD.

The V_2CT_x nanosheets were deposited on CY using an electrophoretic process with some local modifications reported elsewhere.[36] The two electrodes were kept 2 cm apart in the suspension. The EPD was performed by applying a constant DC voltage of +20 V for different iterations such as 10, 20, and 30 min resulting in mass loadings of 0.25, 0.5, and 0.6 mg on the CY substrate, respectively. During the deposition, continuous stirring was applied to the solution to reduce the bubble formation because of water electrolysis, which contributed to homogeneous deposition of the V_2CT_x layer on the surface of the CY wire. We obtained V_2CT_x nanosheets by delaminating multilayered V_2CT_x nanosheets exploiting HF etching to remove Al atoms from the MAX phase of V_2AlC (see Figure 1a). The self-restacking of the V_2CT_x nanosheets and their instability negatively impact the electrochemical properties of the active material. Another problem is the gradual oxidation of the active material, which significantly degrades the electrochemical performance of the material.[38,39] The instability of V_2CT_x under ambient conditions limits its applications, especially in aqueous electrolytes. Here, we describe a modified approach for the fabrication of V_2CT_x-based electrodes with improved electrochemical performance.

Recently, a new approach has been reported to assemble 2D metal oxides keeping layered morphology intact with the assistance of metal cations to synthesize preintercalated oxide active material for energy storage applications.[40] This approach is primarily based on the principle of electrostatic attraction of negatively charged 2D oxide nanosheets to cations, resulting in the synthesis of layered structures with enhanced electrochemical performance. The same approach has been recently reported in the case of MXene where some drops of NaOH were added to $Ti_3C_2T_x$ dispersion that helped in the flocculation of MXene nanoparticles, and porous aggregates with wrinkled morphology were obtained.[41] Here, we established that electrostatic interactions of electrolyte ions (cations) and the V_2CT_x nanosheet can be exploited to make NaOH-driven V_2CT_x dispersion and EPD of the V_2CT_x film on CY. The cation-driven deposition not only enhances the capacitive properties of V_2CT_x but also converts the electrochemical unstable MXene nanosheets into a stable thin film, as demonstrated in Figure 1b. Figure 1c shows an SEM image of the pristine CY. Figure 1d shows the top and cross-sectional views of V_2CT_x nanosheets deposited on the CY. Higher-magnification images in Figure 1e,f show the nanosheets and 2D layer structure of V_2CT_x uniformly deposited on the CY.

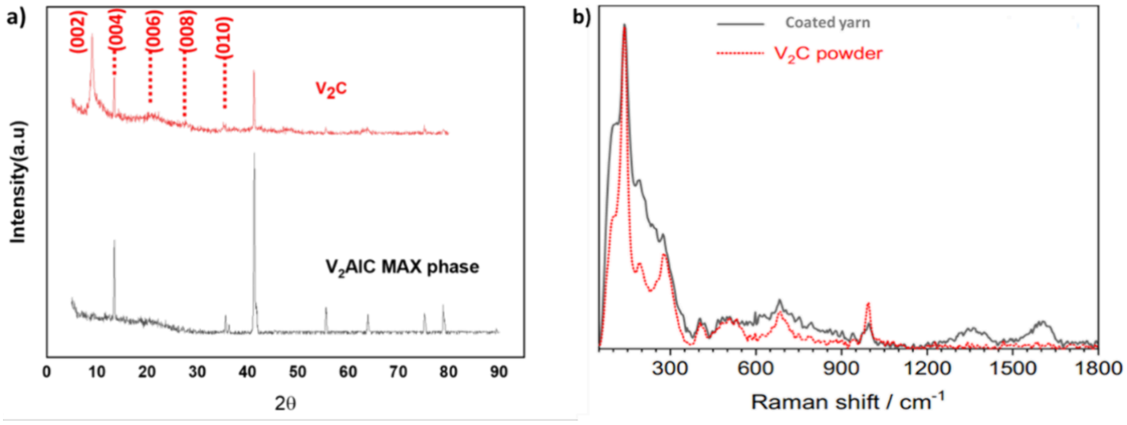

Figure 3. (a) XRD spectra and (b) Raman spectroscopy of deposited 2D MXene (V_2CT_x) carbon yarn.

The inset images (Figure 1f) confirm the material's 2D layered structure, consistent with what is reported in the literature. The EPD films have open structures with higher accessible active sites, which is essential for electrochemical processes, and the DC voltage supplied during EPD offers stronger adhesion of the active material to the substrate (CY). The uniformity of the deposition of V_2CT_x on CY was also investigated by performing an electron-dispersive X-ray (EDX) at different areas on the substrate, as explained by EDX analysis and backscattered images as depicted in Figure 2a,b. The EDX spectra obtained at different areas demonstrated that a thin layer of V_2CT_x is present on a substrate, which is also depicted in backscattered images. The presence of corresponding constituent elements such as carbon, oxygen, and vanadium (as shown in Figure 2c−f) was evenly distributed across the composite film and hence confirmed the even deposition of the V_2CT_x film on the CY wire. However, some agglomerates are sited on a substrate, which can be ascribed to restacking of V_2CT_x nanosheets and unreacted nanosheets owing to poor washing after deposition.

The crystallographic analysis of the as-synthesized samples was performed via X-ray diffraction (XRD). In Figure 3a, the prominent downshift of the (002) peak from $2\theta = 13.49$ to 8.96° in the synthesized V_2CT_x sample indicates the removal of the Al layer with c-lattice expansion, which is very much in line with literature.[42,43] The presence of the (002) peak also indicates that the V_2AlC MAX phase is not completely converted into the V_2CT_x nanosheet during HF etching, and there remain some unreacted V_2AlC particles because according to the literature, the yield after HF treatment at room temperature is around 60%. The post-HF treatment XRD pattern exhibits unreacted V_2AlC together with a new broad peak around 2θ of 8.96°, which is assigned to the (002) plane of MXene.[44] In the case of MXene samples, that shift in the (002) peak may be ascribed to the expansion in the intralayer spaces owing to the abstraction of the Al atoms during the HF etching process, which is also confirmed by Raman spectra as shown in Figure 3b. The red dotted line represents the Raman spectrum obtained from V_2CT_x synthesized powder, produced by etching V_2AlC powder with HF. It helps identify the bands in the spectrum corresponding to the V_2CT_x MXene coating deposited on the yarn for 10 min. Apart from the CY Raman peaks at 1350 and 1597 cm^{-1}, typically attributed to their D and G bands, the spectra closely match. According to ref 45, the ∼280 cm^{-1} peak observed in both Raman spectra in Figure 3b is a characteristic vibrational mode of the V_2CT_x MXene phase that emerges after etching V_2AlC for 10 min. This peak is attributed in ref 45 to the increased interlayer spacing in V_2CT_x MXene compared to bulk V_2AlC, which does not exhibit a peak at this wavenumber in its Raman spectrum.

Also, according to ref 40, broad Raman peaks centered at 405, 510, and 682 cm^{-1} were identified as active vibrational modes of the terminated V_2CT_x MXene phase, with T_x groups being OH, F, and OH, respectively, as predicted by density functional theory calculations.[41] According to theoretical calculations,[46] the peak at ∼405 cm^{-1} corresponds to $V_2C(OH)_2$ and the peaks at ∼520 and ∼690 cm^{-1} to V_2CF_2 and $V_2CO(OH)$, respectively. Therefore, both the Raman and XRD data confirm the successful synthesis of the V_2CT_x MXene phase but terminated with −OH, −F, and −OH groups. The Raman data also suggest that V_2O_5 may have formed and coexisted with the V_2CT_x phase, likely due to oxidation of V_2CT_x MXene into V_2O_5 resulting from the reaction of V_2CT_x with water. Baltakesmez et al.[47] reported a full list of vibration modes for V_2O_5 crystal—140.75, 201.62, 279.92, 403.54, 481.59, 506.54, 692.81, and 996.67 cm^{-1}—and ascribed the peak at 260.75 cm^{-1} to the VO_2 V−O vibrational mode. All of the peaks coincide with those shown in the spectra of Figure 3b. Therefore, the vanadium pentoxide phase should coexist with terminated V_2CT_x where T was identified by Raman to be F and OH groups. This V_2CT_x phase is further confirmed by the Raman characteristic peak at ∼794 cm^{-1}, which is in ref 48 assigned to V_2CT_x with F and OH terminal groups. This peak typically appears below 750 cm^{-1} for V_2C MXene without fluorine and/or hydroxyl terminations, a shift also reported for other MXene. The same composition (i.e., the coexistence of phases) is found for the V_2CT_x-coated yarn. The corresponding Raman spectrum is shown in black in Figure 3b and is identical with that of the V_2CT_x-synthesized powder, demonstrating that the yarn has been successfully coated with V_2CT_x. Compared to the V_2CT_x powder spectrum, the CY spectrum has only two additional peaks at 1365 and 1604 cm^{-1}, which are ascribed to the D and G bands of the CY.[49] The contribution from MXene particles, although possible,[50] is discarded because these C-peaks are not detected in the V_2CT_x powder Raman spectrum.

The primary motivation behind the deposition of V_2CT_x onto CY was to investigate its behavior at different pH levels and identify an optimal potential window for its use as an electrode-active material in batteries and SC devices. To determine the optimal time of deposition and potential

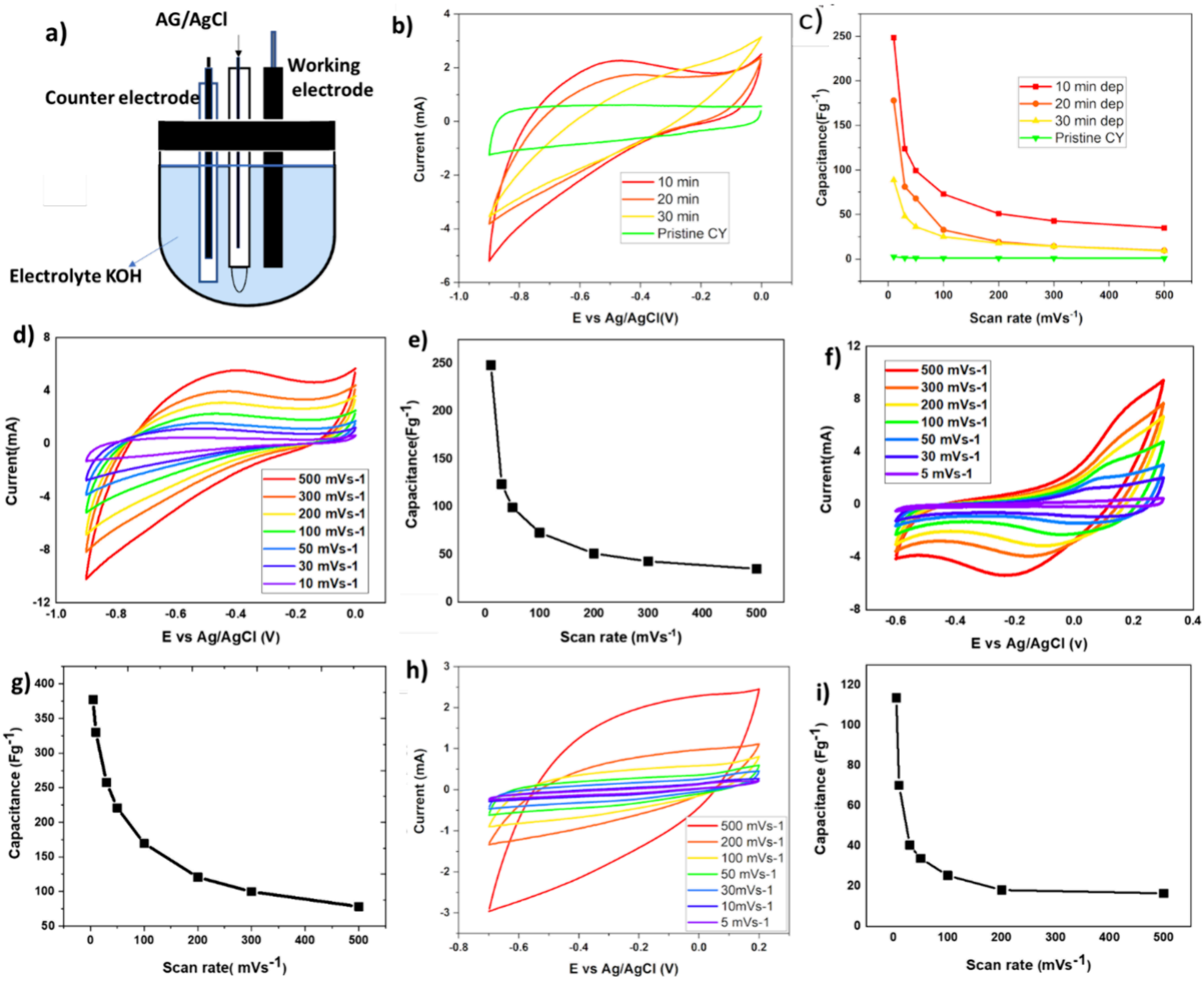

Figure 4. (a) Schematic of the three-electrode setup. (b, c) Comparison of CVs at 100 mV s^{-1} and specific capacitance for 0, 10, 20, and 30 min of deposition of V_2CT_x. (d) CVs recorded at different scan rates for 10 min of deposition. (e) Comparison of specific capacitance at different scan rates. (f, g) CVs and specific capacitances calculated at different scan rates in 1 M H_2SO_4. (h, i) CVs and specific capacitance computed at different scan rates in 1 M Na_2SO_4.

windows of the V_2CT_x-based material, three different electrodes were fabricated with 10, 20, and 30 min and referred to as EPD 10, EPD 20, and EPD 30, respectively. These electrodes were electrochemically characterized in a typical three-electrode setup using 1 M KOH solution as an electrolyte. The V_2CT_x-deposited electrode was the working electrode, the Pt rod was the counter electrode, and Ag/AgCl was the reference electrode, as shown in the schematic in Figure 4a. The electrodes were studied in 1 M KOH solution, and the potential window was set to −0.9 to 0 V. The cyclic voltammograms were recorded for all three electrodes (EPD 10, EPD 20, and EPD 30) at different scan rates in the range 10−500 mV s^{-1}, and specific capacitances were calculated using eqs 1 and 2. The results are shown in Figure 4b,c. The recorded CVs demonstrated quasi-rectangular shapes despite the increase in the scan rate from 10 to 500 mV s^{-1}, revealing that the loaded active material has a good ion response and therefore exhibited good pseudocapacitive behavior. However, the characteristic oxidation/reduction peaks are not evident in CVs, which reveal the ion intercalation and pseudocapacitive behavior of the material. The devices have demonstrated a specific capacitance of 248, 177, and 89 F g^{-1} at 10 mV s^{-1} for 10, 20, and 30 min of deposition, respectively. The electrode fabrication with less time and low mass loading shows the best electrochemical performance and exhibited higher specific capacitance compared with longer time of depositions. This phenomenon can be described as follows: during the deposition, the film thickness generally increases with increasing time of deposition and mass loading, which consequently increases the path length for electrolyte ions and results in reduced ion transportation. This increase in the thickness of the film limits the full exploitation of available active sites of the electrode material and demonstrates a low electrochemical performance in terms of specific capacitances. Clearly, a higher gravimetric capacitance is more appropriate for commercial purposes. Considering the gravimetric capacitances, the V_2CT_x/CY electrode with mass loading 0.25 mg has an optimized electrochemical performance (248 F g^{-1}) for EPD 10, and this optimized time is used for further characterization of the devices in other electrolytes at different

https://doi.org/10.1021/acsomega.4c06035
ACS Omega 2025, 10, 7621−7634

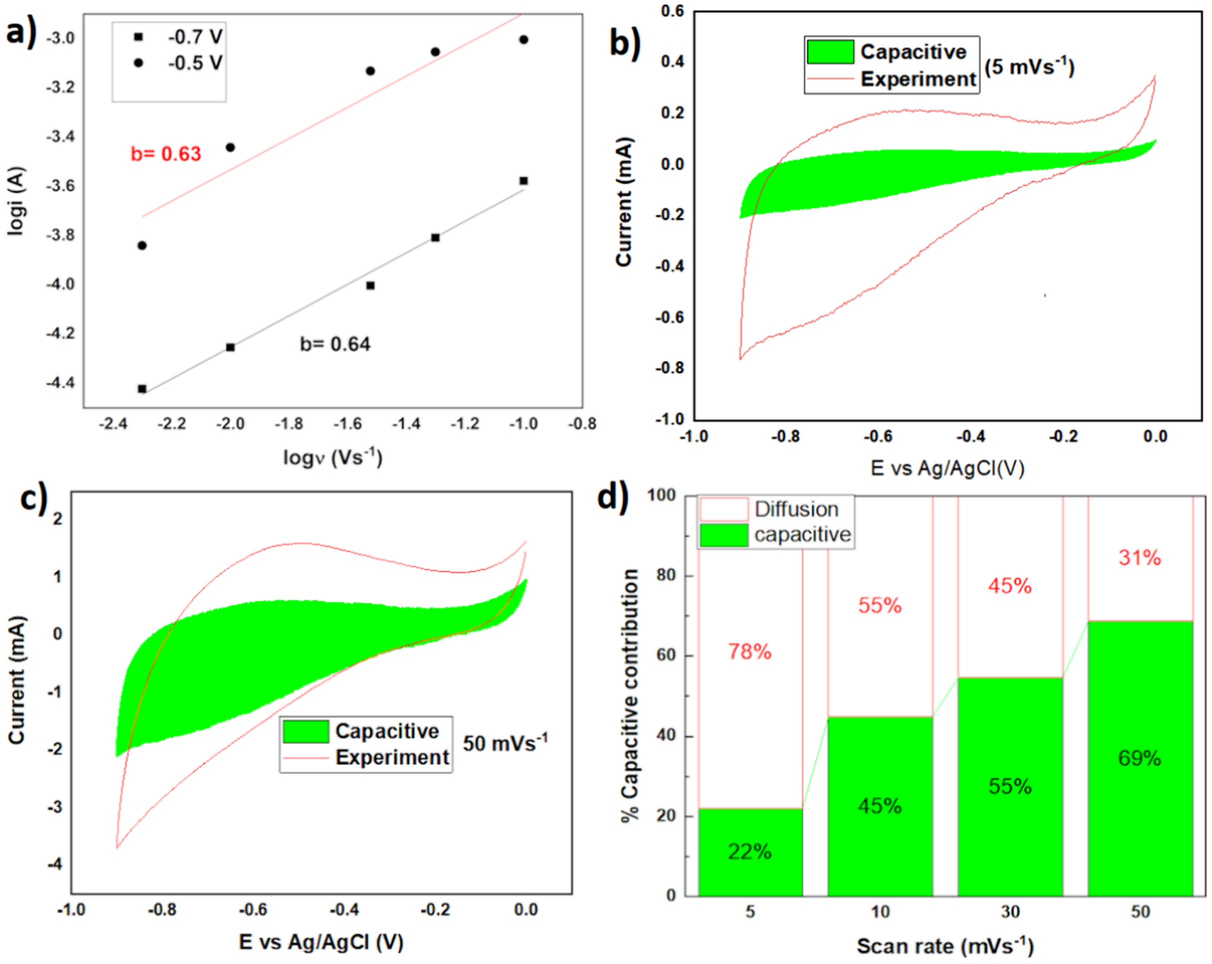

Figure 5. (a) *b*-values at different potential values. (b−d) CVs and percentage capacitive contribution at various scan rates of electrophoretic deposition of 2D MXene (V_2CT_x) carbon yarn in 1 M KOH electrolyte.

pH to better understand the electrochemical behavior of the material and diversity of potential windows for V_2CT_x/CY to be used in energy applications. Therefore, the electrochemical performance of V_2CT_x was also investigated in 1 M H_2SO_4 and 1 M Na_2SO_4 electrolytes. The CVs were recorded at different scan rates ranging 5−500 mV s^{-1} in the potential window of −0.6 to 0.3 and −0.7 to 0.2 V for H_2SO_4 and Na_2SO_4 as depicted in Figure 4f,g and 4h,i, respectively. The respective specific capacitances calculated were also presented. During cycling in 1 M H_2SO_4, the device exhibited very broad redox peaks, observed around 0.1 and −0.2 V vs Ag/AgCl, indicating a redox behavior of V_2CT_x nanosheets in an acidic medium. Similarly, two broad oxidation and reduction peaks were observed on 0.15 and 0−0.2 V vs Ag/AgCl upon cycling in 1 M Na_2SO_4. The indication of the characteristic redox peaks suggests potential electrochemical interactions of electrolyte cations, and peaks represent the conversion of redox couple V^{4+}/V^{3+}.[51]

To confirm the contribution of both capacitive control (due to electric double-layer capacitance EDLC) and diffusion control (pseudocapacitive contribution), further analysis was performed on the CVs recorded at different scan rates. The typical shapes of the CV data recorded at different scan rates showed that oxidation/reduction reactions occur during charging and discharging. Therefore, it can be concluded that an electrochemical reaction also happens during the charging (oxidation reaction) and discharging (reduction reaction) of the V_2CT_x/CY composite electrode in the alkaline electrolyte (1 M KOH). During the electrochemical characterization, typical oxidation/reduction was evidently detected at lower or higher scan rates, as indicated in Figure 4. However, the quasi-rectangular shapes, particularly at lower scan rates, denote the oxidation/reduction reactions in V_2CT_x and are a typical case of pseudocapacitive behavior due to redox coupling (V^{4+}/V^{3+}). At lower scan rates, the ions intercalate into the V_2CT_x nanostructure as they have adequate time to diffuse in the pores of the nanostructure and display a redox reaction (V^{4+}/V^{3+}) by exploiting all the accessible sites of active material. On the contrary, at higher scan rates, the composite electrode demonstrates ideal EDLC behavior and maintains a characteristic shape representative of EDLC behavior, i.e., surface charge storage and hence high-power delivery.

This behavior is evident at a higher scan rate, where electrolyte ions can only have access to the surface of the active material, and a smaller number of available active sites have been occupied during an oxidation/reduction reaction and ion intercalation.

It is important to understand how pseudocapacitive materials store charges during electrochemical characterization. It is well known that metal oxides/carbides store energy by exploiting both faradaic and non-faradaic reactions. In EDL capacitors, the non-Faradaic charge storage mechanism is the dominant factor. In the incumbent mechanism, energy is

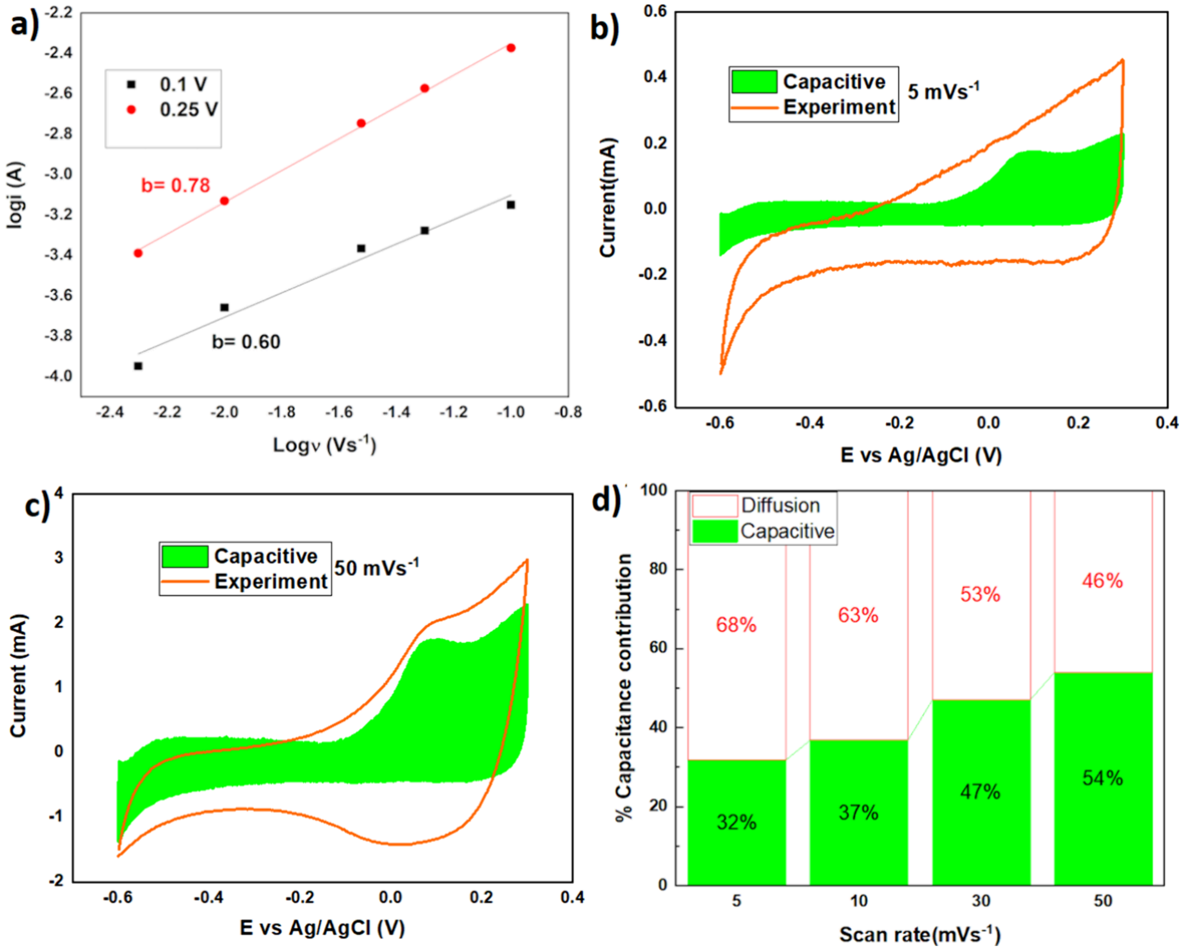

Figure 6. (a) *b*-values at different potential values. (b–d) CVs and percentage capacitive contribution at various scan rates of electrophoretic deposition of 2D MXene (V_2CT_x) carbon yarn in 1 M H_2SO_4 electrolyte.

stored electrostatically from the surface reversible adsorption/desorption of charge on high surface area materials. On the other hand, Faradaic reactions can occur both on the surface normally exhibiting redox pseudocapacitance and in the bulk of the active material representative of battery-like behavior, i.e., diffusion controlled.[52] It is reported that when the active material dimension decreases to the nanoscale level, the material exhibits both charge storage effects, that is, diffusion controlled, as well as double-layer capacitance. The quantitative contribution of both effects can be determined by investigating the CVs recorded at different sweep rates by using the Dunn formula.

$$i = a\nu^{b} \tag{3}$$

The above mathematical model demonstrates that the current, *i*, obeys a power law link with the sweep rates, and *ν*, *a*, and *b* are variable parameters, taking the logarithmic function of both sides of eq 3:

$$\log i = b \times \log a + \log \nu \tag{4}$$

In general, the value of *b* varies between 0.5 and 1. When the *b* value is close to 1, it implies that the energy is stored through a surface charge storage mechanism, that is, capacitive contribution. When the *b* value approaches 0.5, it indicates that the current varies with the square root of the sweep rate, representing that the charge stored follows an ideal diffusion-controlled process. The calculated *b* values for the V_2CT_x/CY electrodes are shown in Figures 5–7. Figures 5a, 6a, and 7a also show two plots of log(i) vs log(ν) exhibiting two different *b* values 0.63 and 0.64 at random potentials of −0.7 and −0.5 V, respectively, 0.78 and 0.60 at 0.1 and 0.25 V, respectively, and 0.71 and 0.82 at −0.1 and −0.15 V, respectively. During scanning in different potential windows vs Ag/AgCl, it is found that the value of *b* always varies between 0.5 and 1, implying that material stores charges using both the charge-accumulating processes EDLC and the intercalation. This indicates that the V_2CT_x/CY composite electrode exhibits both pseudocapacitive and ELDC behavior. To further calculate the quantitative contribution of charge storage in the V_2CT_x/CY electrode; the total charge stored is divided into two categories, Faradaic or intercalation contribution (diffusion controlled) and EDL effect (capacitive contribution) according to Dunn et al.[53] Therefore, for any material, current response, *i*, at a fixed voltage, *V*, can be calculated as the sum of capacitive contribution $k_1\upsilon$ (usually associated with EDL) and the Faradaic/intercalation process (typically representative of pseudocapacitance) $k_2\nu^{1/2}$:

$$i(V) = k_1\upsilon + k_2\nu^{1/2} \tag{5}$$

Thus, the above equation after rearrangement can also be written as follows:

$$i(V)/\nu^{1/2} = k_1\nu^{1/2} + k_2 \tag{6}$$

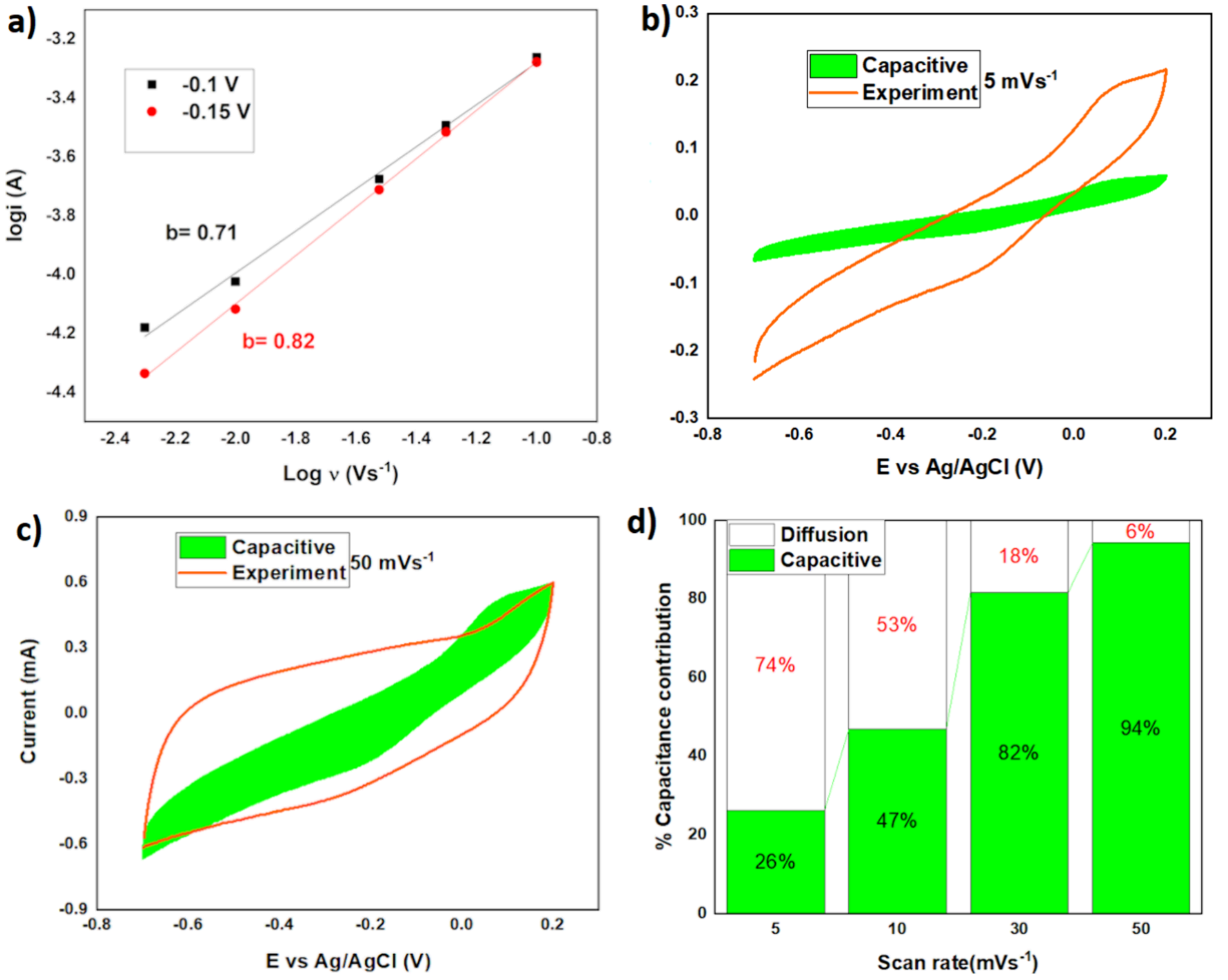

Figure 7. (a) *b* values at different potential values. (b−d) CVs and % capacitive contribution at different scan rates of electrophoretic deposition of 2D MXene (V_2CT_x) carbon yarn in 1 M Na_2SO_4 electrolyte.

k_1 and k_2 calculate the capacitive and diffusion contributions of the current at fixed potentials. This is consistent with the calculation of current arising from the intercalation of cations such as K^+, H^+, and Na^+ and the current resulting from the EDL process and the corresponding percentage contributions to the total charge accumulation. Figures 5−7b−d depict the contribution of EDL and the Faradaic process to the total charge accumulation of the V_2CT_x-based electrode. The particular interest of the material under investigation is to study the charge accumulation mechanism of the V_2CT_x/CY composite electrode at higher sweep rates, since SCs have an advantage over batteries of being able to rapidly charge/discharge and deliver high-power throughput. However, V_2CT_x thin-film deposition on flexible electrodes showed a diffusion contribution at a higher scan rate of 50 mV s^{-1} accounting for 31, 46, and 6% of the total charge stored in 1 M KOH, H_2SO_4, and Na_2SO_4, respectively. The material has shown good rate capability in KOH and H_2SO_4 where nearly half of the charge is stored due to ion intercalation (diffusion controlled), especially in acidic medium, 1/3 contribution in case of basic medium, but less in neutral electrolyte. Furthermore, pseudocapacitive behavior becomes more prominent with around 75% of the total charge accumulated at lower scan rates.

In terms of electrochemical performance, the V_2CT_x/CY electrode has demonstrated excellent electrochemical performance in all three electrolytes, and the device has exhibited higher gravimetric capacitance of 377 F g^{-1} at 5 mV s^{-1} in 1 M H_2SO_4 as shown in Figure 8a, and this performance is compared to other vanadium carbide electrodes, as shown in Table 1. The demonstrated electrochemical performance is higher than the similar MXene families such as Ti_3C_2,[54] Mo1.33C,[55] Mo_2C,[56] and $V_4C_3T_x$[57] in 1 M H_2SO_4 electrolyte, which can be attributed to the lower molar mass of V_2CT_x. The specific capacitances decreased to 221 and 169 F g^{-1} at 50 and 100 mV s^{-1}, respectively, demonstrating the acceptable rate capability of the material. Higher mass loading could cause restacking of the nanosheets, limit the electrolyte accessibility to the active sites, and degrade the electrochemical performance of the composite electrode. To explore the prospective applicability of the V_2CT_x/CY electrode as an anode material for asymmetric SCs, the aging of V_2CT_x/CY was tested by performing CV at 100 mVs^{-1} for 3000 cycles, as shown in Figure 8b. The device has shown excellent cyclic stability in all three electrolytes with capacitance retentions of 87, 95, and 91%. Still, the device showed relatively more electrochemical degradation in H_2SO_4 as compared to other electrolytes, which agrees with the literature as shown in Table 2.

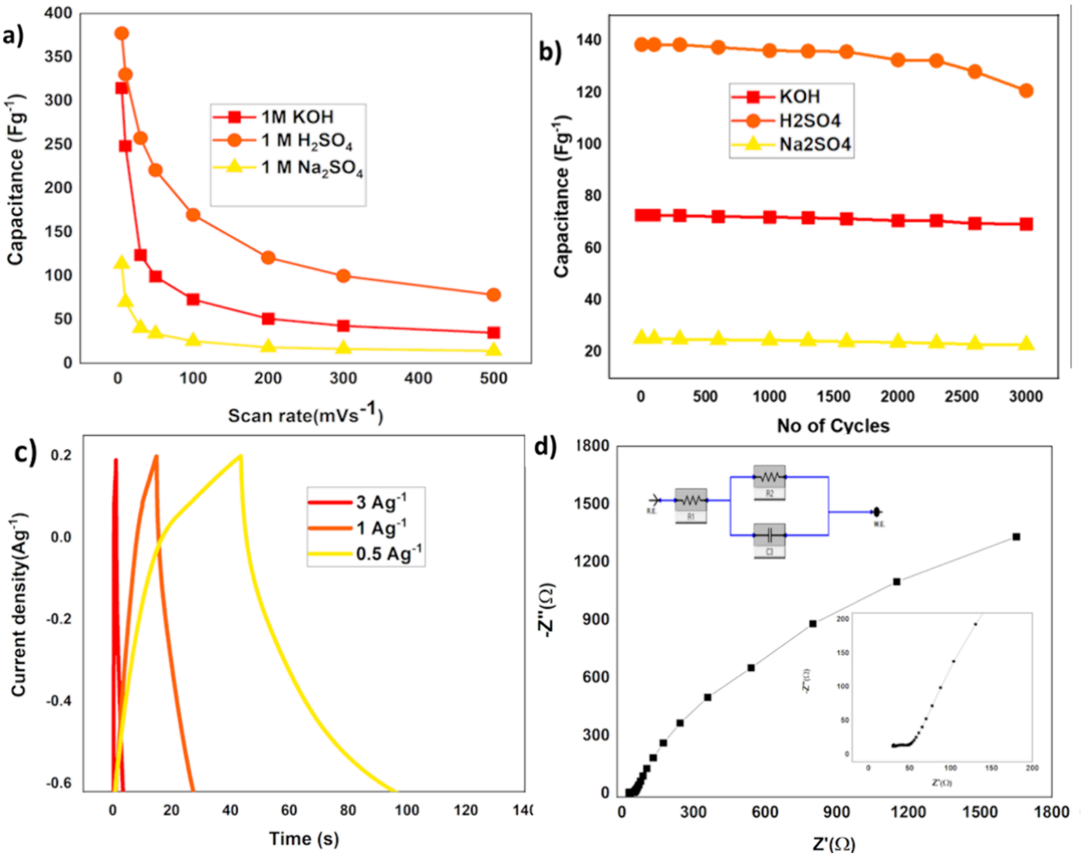

Figure 8. (a) Comparison of specific capacitance in different electrolytes, (b) comparison of cyclic stability of devices in different electrolytes, (c) comparison of galvanostatic charge and discharge curve obtained at different current densities, (d) Nyquist graph of V_2CT_x/CY with a changing frequency from 0.01 to 100,000 Hz (inset figure illustrates the zoomed Nyquist plots in the high-frequency zone and equivalent circuit).

Table 1. Comparison of Performance with V_2CT_x-Based Electrodes

Sr#	MXene material	composite or doped	binder used fabrication	configuration	electrolyte	potential window (V)	capacitance F g^{-1}	ref.
1	V_4C_3	plain material	Nafion	three electrodes	1 M H_2SO_4	−0.4 to +0.4 V	330 F g^{-1} at 5 mV s^{-1}	57
2	V_4C_3	plain material	PVDF	three electrodes	1 M H_2SO_4	−0.35 to 0.15 V	286.5 F g^{-1} at 2 mV s^{-1}	58
3	V_4C_3 T_x	N-doped	PVDF	three electrodes	1 M H_2SO_4	−0.2 to 0.4 V	210 F g^{-1} at 10 mV s^{-1}	59
4	V_2C	plain material	binder free	three electrodes	1 M H_2SO_4	−1.1 to 0.5 V	487 F g^{-1} at 2 mV s^{-1}	60
5	V_2C	plain material	binder free	Swagelok cell	1 M KOH	−1.2 to 0.6 V	184 F g^{-1} at 2 mV s^{-1}	42
6	V_2CT_x	V_2CT_x/CY	binder free	three electrodes	1 M KOH	−0.9 to 0 V	248 F g^{-1} at 5 mV s^{-1}	our work
7	V_2C T_x	V_2CT_x/CY	binder free	three electrodes	1 M H_2SO_4	−0.6 to 0.4 V	377 F g^{-1} at 5 mV s^{-1}	our work

Table 2. Comparison of Cyclic Stability Performance

Sr#	material	substrate or current collector	electrolyte	no. of cycles	capacitance retentions %	ref.
1	Ta_4CT_x	carbon paper	1 M H_2SO_4	2000	89	61
2	$Ti_3C_2T_x$	PET substrate	6 M KOH		46	62
3	$Ti_3C_2T_x$	PP substrate	6 M KOH		73.3	62
4	$Ti_3C_2T_x$	graphite	6 M KOH	3000	92	63
5	$Ti_3C_2T_x$	glass	6 M KOH	3000	82	63
6	MWCNT@V_2CT_x	Ni foam	1 M KOH	10000	94	64
7	V_2CT_x		seawater	5000	89.1	65
8	V_2CT_x/CY	carbon yarn wires	1 M KOH	3000	95	this work
9	V_2CT_x/CY	carbon yarn wires	1 M H_2SO_4	3000	87	this work
10	V_2CT_x/CY	carbon yarn wires	1 M Na_2SO_4	3000	91	this work

Pseudocapacitive materials such as vanadium oxides often have a cyclic stability problem compared to carbonaceous materials, which often rely on the EDL mechanism. The apparent loss of capacitance in acidic media is attributed to partially irreversible redox reactions and potential oxidation, causing carbide degradation. Constant current galvanostatic charging and discharging were also performed on the V_2CT_x/CY electrode at different current densities, which show minor deviations from the typical triangular curves, as shown in Figure 8c. This nonlinear behavior of the GCD curves in the absence of a plateau indicates that V_2CT_x/CY charge storage is pseudocapacitive in nature, and this pseudocapacitive charge storage mechanism causes them to deviate from traditional triangular shapes, which are attributed to surface charge storage or EDL. Typically, at a low current density, the GCD curve exhibits mixed behavior, which is a combination of electric double layer (EDL) and pseudocapacitance. Initially, it starts with EDLC's typical triangular charge and discharge curve followed by pseudocapacitive discharge status.[65,66]

This specific charge storage behavior is mainly ascribed to the large surface area of composite electrodes of V_2CT_x/CY that could exhibit higher EDLC capacitance, especially for highly porous MXene-based composite electrodes. However, during the discharging process, EDLC discharge demonstrates a quick potential drop followed by the phase transformation with an extended discharging time owing to the diffusion of electrolyte ions in the bulk structure of active material for redox couple. Contrarily, at higher current densities, the GCDs exhibited a typical triangular behavior attributed to quick charge and discharge and surface charge storage mechanisms and limited redox reactions. These observations are consistent with GCD curves for MXene materials, as reported in many studies of MXene materials for SC applications.[61,65,67−72] This requires further in operando investigation such as in situ XRD or Raman analysis about the electrochemical stability of the vanadium carbide. There may be more than one possible explanation for this unusual behavior such as the creation of an extra electrolyte/electrode interface, the intercalation of ions into the structure of the material, and the material lacking full reversibility and trapping some of the cations in the V_2CT_x layer structure. Another possible reason could be the potential dissolution and decomposition of vanadium and functional groups (formed during MXene synthesis) during electrochemical cycling, causing this asymmetric curve behavior.[57,73,74] Furthermore, EIS was performed in the frequency range of 10 mHz to 1 MHz to analyze and understand the kinetic behavior of the synthesized V_2CT_x/CY electrode in the bulk of aqueous electrolyte. The Nyquist plot for the composite material (V_2CT_x/CY) is shown in Figure 8d in the KOH electrolyte. The vertical line in the low-frequency region of the Nyquist plot is ascribed to the slower diffusion process of electrolyte ions into V_2CT_x nanosheets and the capacitive nature of the CY wire. The privation of a typical semicircle radius in the high-frequency region of the plot and the lower value of charge transfer resistance demonstrate the high conductivity of the V_2CT_x nanosheets. The equivalent circuit model was also fitted with the experimental EIS data, and it is possible to determine the highest frequencies of uncompensated resistance attributed to material interfaces and the lower frequencies of constant phase element that represent EDLC and pseudocapacitance and medium-frequency Warburg impedance, which describes the diffusion-controlled behavior of the material. The uncompensated resistance of V_2CT_x nanosheets is 32 Ω, and the charge transfer resistance of 16 Ω can be attributed to the bulk of the aqueous electrolyte. The EIS plot illustrates that the resistance of the bulk electrolyte has a significant role in charge transfer.

■ CONCLUSIONS

In summary, a facile EPD strategy has been employed for the fabrication of binder-free V_2CT_x/CY -based SCs with remarkable capacitive performances. The main novelty and uniqueness are the exploitation of a green, time-saving, and scalable technique for binder-free deposition of the layered structure of V_2CT_x with controlled and uniform mass loading on flexible substrates, without loss of electrochemical performance as compared with other methods. The EPD method supports the deposition of a layered and interconnected framework of V_2CT_x nanostructure with uniform and wide pore size distribution, confirming the improved electrochemical performance owing to increased approachability of electrolyte ions to the pores of active material. This study has shown that the electrochemical behavior of V_2CT_x is pH sensitive exhibiting a maximum capacitance of 377 F g^{-1} in an acidic medium, i.e., H_2SO_4 aqueous electrolyte. The device has also demonstrated a good rate capability and good diffusion-controlled electrochemical behavior even at higher scan rates encouraging further exploration of V_2CT_x material in batteries and SCs. The capacitive performance of V_2CT_x can be further enhanced by compositing this material with some other redox materials, exploring different arrangements such as hydrogels, vertical layer orientations, or hybridization with other redox particles. Finally, the understanding of the capacitive and diffusion control behavior at different pH levels will open a new aspect to explore different applications of V_2CT_x such as anode active flexible lithium-ion batteries and high energy density asymmetric SCs in both aqueous and organic electrolytes. For precisely accessing electrode bending stability on this highly flexible substrate, further tests are being conducted on new asymmetric SC devices that exploit the material herein characterized as anode.

■ AUTHOR INFORMATION

Corresponding Authors

Amjid Rafique − *CENIMAT|I3N, Materials Science Department, NOVA School of Science and Technology, (NOVA FCT) University of Lisbon, 2829-516 Caparica, Portugal;* orcid.org/0000-0001-9508-0864; Email: a.rafique@fct.unl.pt

Ana Catarina Baptista − *CENIMAT|I3N, Materials Science Department, NOVA School of Science and Technology, (NOVA FCT) University of Lisbon, 2829-516 Caparica, Portugal;* orcid.org/0000-0003-1631-6248; Email: anacbaptista@fct.unl.pt

Authors

Usman Naeem − *Physics Characterization and Simulation Lab, Department of Physics, School of Natural Sciences (SNS), National University of Science and Technology (NUST), Islamabad 44000, Pakistan*

Ana Marques − *CENIMAT|I3N, Materials Science Department, NOVA School of Science and Technology, (NOVA FCT) University of Lisbon, 2829-516 Caparica, Portugal; Physics Department, Faculty of Sciences, University of Lisbon, 1749-016 Lisbon, Portugal*

Isabel Ferreira − *CENIMAT|I3N, Materials Science Department, NOVA School of Science and Technology, (NOVA FCT) University of Lisbon, 2829-516 Caparica, Portugal;* orcid.org/0000-0002-8838-0364

Syed Rizwan − *Physics Characterization and Simulation Lab, Department of Physics, School of Natural Sciences (SNS), National University of Science and Technology (NUST), Islamabad 44000, Pakistan;* orcid.org/0000-0002-6934-0949

Complete contact information is available at:
https://pubs.acs.org/10.1021/acsomega.4c06035

Notes

The authors declare no competing financial interest.

■ ACKNOWLEDGMENTS

This work was financed by national funds from FCT - Fundação para a Ciência e a Tecnologia, I.P., in the scope of the All-FIBRE project with the reference PTDC/CTM-CTM/1571/2020, and the projects LA/P/0037/2020, UIDP/50025/2020UIDP/50025/2020, and UIDB/50025/2020 of the Associate Laboratory Institute of Nanostructures, Nano modelling, and Nanofabrication−i3N. Nanofabrication—i3N. Syed Rizwan thanks the Higher Education Commission (HEC) of Pakistan for providing research funding under the Project No. 20-14784/NRPU/R&D/HEC/2021.

■ REFERENCES

(1) Balasingham, K. *Industry 4.0: securing the future for German manufacturing companies*. Master's thesis, University of Twente 2016.

(2) Unit, E. I., The Internet of Things business index: a quiet revolution gathers pace. *Economist*, **2013**.

(3) Datta, S. K.; Bonnet, C. MEC and IoT based automatic agent reconfiguration in industry 4.0. in *2018 IEEE International Conference on Advanced Networks and Telecommunications Systems (ANTS)*. 2018, IEEE.

(4) Hossein Motlagh, N.; Mohammadrezaei, M.; Hunt, J.; Zakeri, B. Internet of Things (IoT) and the energy sector. *Energies* **2020**, *13* (2), 494.

(5) Lethien, C.; Le Bideau, J.; Brousse, T. Challenges and prospects of 3D micro-supercapacitors for powering the internet of things. *Energy Environ. Sci.* **2019**, *12* (1), 96−115.

(6) Sheberla, D.; Bachman, J. C.; Elias, J. S.; Sun, C.-J.; Shao-Horn, Y.; Dincă, M. Conductive MOF electrodes for stable supercapacitors with high areal capacitance. *Nature materials* **2017**, *16* (2), 220−224.

(7) Simon, P.; Gogotsi, Y. Materials for electrochemical capacitors. *Nature materials* **2008**, *7* (11), 845−854.

(8) Stoller, M. D.; Ruoff, R. S. Best practice methods for determining an electrode material's performance for ultracapacitors. *Energy Environ. Sci.* **2010**, *3* (9), 1294−1301.

(9) Persson, I.; El Ghazaly, A.; Tao, Q.; Halim, J.; Kota, S.; Darakchieva, V.; Palisaitis, J.; Barsoum, M. W.; Rosen, J.; Persson, P. O. Tailoring structure, composition, and energy storage properties of MXenes from selective etching of in-plane, chemically ordered MAX phases. *Small* **2018**, *14* (17), No. 1703676.

(10) Zhao, S.; Kang, W.; Xue, J. MXene nanoribbons. *Journal of Materials Chemistry C* **2015**, *3* (4), 879−888.

(11) Zhao, M.-Q.; Torelli, M.; Ren, C. E.; Ghidiu, M.; Ling, Z.; Anasori, B.; Barsoum, M. W.; Gogotsi, Y. 2D titanium carbide and transition metal oxides hybrid electrodes for Li-ion storage. *Nano Energy* **2016**, *30*, 603−613.

(12) Yu, Z.; Tetard, L.; Zhai, L.; Thomas, J. Supercapacitor electrode materials: nanostructures from 0 to 3 dimensions. *Energy Environ. Sci.* **2015**, *8* (3), 702−730.

(13) Geim, A. K.; Novoselov, K. S. The rise of graphene. *Nature materials* **2007**, *6* (3), 183−191.

(14) Stoller, M. D.; Park, S.; Zhu, Y.; An, J.; Ruoff, R. S. Graphene-based ultracapacitors. *Nano Lett.* **2008**, *8* (10), 3498−3502.

(15) Vivekchand, S.; Rout, C. S.; Subrahmanyam, K.; Govindaraj, A.; Rao, C. N. R. Graphene-based electrochemical supercapacitors. *Journal of Chemical Sciences* **2008**, *120*, 9−13.

(16) Dong, Y.; Wu, Z.-S.; Ren, W.; Cheng, H.-M.; Bao, X. Graphene: a promising 2D material for electrochemical energy storage. *Science Bulletin* **2017**, *62* (10), 724−740.

(17) Zhao, M. Q.; Ren, C. E.; Ling, Z.; Lukatskaya, M. R.; Zhang, C.; Van Aken, K. L.; Barsoum, M. W.; Gogotsi, Y. Flexible MXene/carbon nanotube composite paper with high volumetric capacitance. *Advanced materials* **2015**, *27* (2), 339−345.

(18) Liu, Y.; Tang, Q.; Xu, M.; Ren, J.; Guo, C.; Chen, C.; Geng, W.; Lei, W.; Zhao, X.; Liu, D. Efficient mechanical exfoliation of MXene nanosheets. *Chemical Engineering Journal* **2023**, *468*, No. 143439.

(19) Urbankowski, P.; Anasori, B.; Makaryan, T.; Er, D.; Kota, S.; Walsh, P. L.; Zhao, M.; Shenoy, V. B.; Barsoum, M. W.; Gogotsi, Y. Synthesis of two-dimensional titanium nitride Ti 4 N 3 (MXene). *Nanoscale* **2016**, *8* (22), 11385−11391.

(20) MR, L.A.A.M.L.; Boson, A.; Gogotsi, Y.; Sinitskii, A. Adv. Electron. *Mater.* **2016**, 2 (12), No. 1600255.

(21) Haider, W. A.; Tahir, M.; He, L.; Mirza, H.; Zhu, R.; Han, Y.; Mai, L. Structural engineering and coupling of two-dimensional transition metal compounds for micro-supercapacitor electrodes. *ACS Central Science* **2020**, *6* (11), 1901−1915.

(22) Ghidiu, M.; Lukatskaya, M. R.; Zhao, M.-Q.; Gogotsi, Y.; Barsoum, M. W. Conductive two-dimensional titanium carbide 'clay'with high volumetric capacitance. *Nature* **2014**, *516* (7529), 78−81.

(23) Hu, T.; Hu, M.; Li, Z.; Zhang, H.; Zhang, C.; Wang, J.; Wang, X. Interlayer coupling in two-dimensional titanium carbide MXenes. *Phys. Chem. Chem. Phys.* **2016**, *18* (30), 20256−20260.

(24) Naguib, M.; Kurtoglu, M.; Presser, V.; Lu, J.; Niu, J.; Heon, M.; Hultman, L.; Gogotsi, Y.; Barsoum, M. W. Two-dimensional nanocrystals: Two-dimensional nanocrystals produced by exfoliation of Ti3AlC2 (Adv. Mater. 37/2011). *Adv. Mater.* **2011**, *23* (37), 4207−4207.

(25) Wang, H.; Wu, Y.; Yuan, X.; Zeng, G.; Zhou, J.; Wang, X.; Chew, J. W. Clay-inspired MXene-based electrochemical devices and photo-electrocatalyst: state-of-the-art progresses and challenges. *Adv. Mater.* **2018**, *30* (12), No. 1704561.

(26) Xie, X.; Zhao, M.-Q.; Anasori, B.; Maleski, K.; Ren, C. E.; Li, J.; Byles, B. W.; Pomerantseva, E.; Wang, G.; Gogotsi, Y. Porous heterostructured MXene/carbon nanotube composite paper with high volumetric capacity for sodium-based energy storage devices. *Nano Energy* **2016**, *26*, 513−523.

(27) Liu, X.; Qian, T.; Xu, N.; Zhou, J.; Guo, J.; Yan, C. Preparation of on chip, flexible supercapacitor with high performance based on electrophoretic deposition of reduced graphene oxide/polypyrrole composites. *Carbon* **2015**, *92*, 348−353.

(28) Javed, M. S.; Dai, S.; Wang, M.; Xi, Y.; Lang, Q.; Guo, D.; Hu, C. Faradic redox active material of Cu 7 S 4 nanowires with a high conductance for flexible solid state supercapacitors. *Nanoscale* **2015**, *7* (32), 13610−13618.

(29) Xia, X.; Zhang, Y.; Chao, D.; Xiong, Q.; Fan, Z.; Tong, X.; Tu, J.; Zhang, H.; Fan, H. J. Tubular TiC fibre nanostructures as supercapacitor electrode materials with stable cycling life and wide-temperature performance. *Energy Environ. Sci.* **2015**, *8* (5), 1559−1568.

(30) Hu, M.; Li, Z.; Zhang, H.; Hu, T.; Zhang, C.; Wu, Z.; Wang, X. Self-assembled Ti3C2Tx MXene film with high gravimetric capacitance. *Chem. Commun.* **2015**, *51* (70), 13531−13533.

(31) Zhu, G.; Pan, L.; Lu, T.; Xu, T.; Sun, Z. Electrophoretic deposition of reduced graphene-carbon nanotubes composite films as counter electrodes of dye-sensitized solar cells. *J. Mater. Chem.* **2011**, *21* (38), 14869−14875.

(32) Du, C.; Pan, N. High power density supercapacitor electrodes of carbon nanotube films by electrophoretic deposition. *Nanotechnology* **2006**, *17* (21), 5314.

(33) Bak, S.-M.; Qiao, R.; Yang, W.; Lee, S.; Yu, X.; Anasori, B.; Lee, H.; Gogotsi, Y.; Yang, X.-Q. Na-ion intercalation and charge storage mechanism in 2D vanadium carbide. *Adv. Energy Mater.* **2017**, *7* (20), No. 1700959.

(34) Zhao, M.-Q.; Xie, X.; Ren, C. E.; Makaryan, T.; Anasori, B.; Wang, G.; Gogotsi, Y. Hollow MXene spheres and 3D macroporous MXene frameworks for Na-ion storage. *Adv. Mater.* **2017**, *29* (37), No. 1702410.

(35) Li, J.; Wang, R.; Zhang, D.; Su, Z.; Li, H.; Yan, Y. Copper Iodide (CuI) coating as a self-cleaning adsorbent for highly efficient dye removal. *J. Alloys Compd.* **2019**, *774*, 191−200.

(36) Hu, Y.; Pang, S.; Li, J.; Jiang, J.; Papageorgiou, D. G. Enhanced interfacial properties of hierarchical MXene/CF composites via low content electrophoretic deposition. *Composites Part B: Engineering* **2022**, *237*, No. 109871.

(37) Rafique, A.; Bianco, S.; Fontana, M.; Pirri, C. F.; Lamberti, A. Flexible wire-based electrodes exploiting carbon/ZnO nanocomposite for wearable supercapacitors. *Ionics* **2017**, *23* (7), 1839−1847.

(38) Xie, Y.; Dall'Agnese, Y.; Naguib, M.; Gogotsi, Y.; Barsoum, M. W.; Zhuang, H. L.; Kent, P. R. Prediction and characterization of MXene nanosheet anodes for non-lithium-ion batteries. *ACS Nano* **2014**, *8* (9), 9606−9615.

(39) VahidMohammadi, A.; Hadjikhani, A.; Shahbazmohamadi, S.; Beidaghi, M. Two-dimensional vanadium carbide (MXene) as a high-capacity cathode material for rechargeable aluminum batteries. *ACS Nano* **2017**, *11* (11), 11135−11144.

(40) Lim, J.; Jin, X.; Jo, Y. K.; Lee, S.; Hwang, S. J. Kinetically controlled layer-by-layer stacking of metal oxide 2D nanosheets. *Angew. Chem.* **2017**, *129* (25), 7199−7202.

(41) VahidMohammadi, A.; Mojtabavi, M.; Caffrey, N. M.; Wanunu, M.; Beidaghi, M. Assembling 2D MXenes into highly stable pseudocapacitive electrodes with high power and energy densities. *Adv. Mater.* **2019**, *31* (8), No. 1806931.

(42) Shan, Q.; Mu, X.; Alhabeb, M.; Shuck, C. E.; Pang, D.; Zhao, X.; Chu, X.-F.; Wei, Y.; Du, F.; Chen, G. Two-dimensional vanadium carbide (V2C) MXene as electrode for supercapacitors with aqueous electrolytes. *Electrochem. Commun.* **2018**, *96*, 103−107.

(43) Zahra, S. A.; Ceesay, E.; Rizwan, S. Zirconia-decorated V2CTx MXene electrodes for supercapacitors. *Journal of Energy Storage* **2022**, *55*, No. 105721.

(44) Naguib, M.; Halim, J.; Lu, J.; Cook, K. M.; Hultman, L.; Gogotsi, Y.; Barsoum, M. W. New two-dimensional niobium and vanadium carbides as promising materials for Li-ion batteries. *J. Am. Chem. Soc.* **2013**, *135* (43), 15966−15969.

(45) Guan, Y.; Jiang, S.; Cong, Y.; Wang, J.; Dong, Z.; Zhang, Q.; Yuan, G.; Li, Y.; Li, X. A hydrofluoric acid-free synthesis of 2D vanadium carbide (V2C) MXene for supercapacitor electrodes. *2D Materials* **2020**, *7* (2), No. 025010.

(46) Champagne, A.; Shi, L.; Ouisse, T.; Hackens, B.; Charlier, J.-C. Electronic and vibrational properties of V 2 C-based MXenes: From experiments to first-principles modeling. *Phys. Rev. B* **2018**, *97* (11), No. 115439.

(47) Baltakesmez, A.; Aykaç, C.; Güzeldir, B. Phase transition and changing properties of nanostructured V 2 O 5 thin films deposited by spray pyrolysis technique, as a function of tungsten dopant. *Appl. Phys. A: Mater. Sci. Process.* **2019**, *125*, 441.

(48) Thakur, R.; VahidMohammadi, A.; Moncada, J.; Adams, W. R.; Chi, M.; Tatarchuk, B.; Beidaghi, M.; Carrero, C. A. Insights into the thermal and chemical stability of multilayered V 2 CT x MXene. *Nanoscale* **2019**, *11* (22), 10716−10726.

(49) Lima, N.; Baptista, A. C.; Faustino, B. M. M.; Taborda, S.; Marques, A.; Ferreira, I. Carbon threads sweat-based supercapacitors for electronic textiles. *Sci. Rep.* **2020**, *10* (1), 7703.

(50) Thakur, R.; Vahid Mohammadi, A.; Moncada, J.; Adams, W. R.; Chi, M.; Tatarchuk, B.; Beidaghi, M.; Carrero, C. A. *Nanoscale* **2019**, *11*, 10716−10726.

(51) Ji, X.; Xu, K.; Chen, C.; Zhang, B.; Wan, H.; Ruan, Y.; Miao, L.; Jiang, J. Different charge-storage mechanisms in disulfide vanadium and vanadium carbide monolayer. *Journal of Materials Chemistry A* **2015**, *3* (18), 9909−9914.

(52) Moniz, M. P.; Rafique, A.; Carmo, J.; Oliveira, J. P.; Marques, A.; Ferreira, I. M.; Baptista, A. C. Electrospray Deposition of PEDOT: PSS on Carbon Yarn Electrodes for Solid-State Flexible Supercapacitors. *ACS Appl. Mater. Interfaces* **2023**, 30727.

(53) Brezesinski, T.; Wang, J.; Tolbert, S. H.; Dunn, B. Ordered mesoporous α-MoO3 with iso-oriented nanocrystalline walls for thin-film pseudocapacitors. *Nature materials* **2010**, *9* (2), 146−151.

(54) Dall'Agnese, Y.; Lukatskaya, M. R.; Cook, K. M.; Taberna, P.-L.; Gogotsi, Y.; Simon, P. High capacitance of surface-modified 2D titanium carbide in acidic electrolyte. *Electrochem. Commun.* **2014**, *48*, 118−122.

(55) Halim, J.; Kota, S.; Lukatskaya, M. R.; Naguib, M.; Zhao, M.-Q.; Moon, E. J.; Pitock, J.; Nanda, J.; May, S. J.; Gogotsi, Y.; Barsoum, M. W. Synthesis and characterization of 2D molybdenum carbide (MXene). *Adv. Funct. Mater.* **2016**, *26* (18), 3118−3127.

(56) Tao, Q.; Dahlqvist, M.; Lu, J.; Kota, S.; Meshkian, R.; Halim, J.; Palisaitis, J.; Hultman, L.; Barsoum, M. W.; Persson, P. O. Å.; Rosen, J. 33C MXene with divacancy ordering prepared from parent 3D laminate with in-plane chemical ordering. *Nat. Commun.* **2017**, *8* (1), 14949.

(57) Syamsai, R.; Grace, A. N. Synthesis, properties and performance evaluation of vanadium carbide MXene as supercapacitor electrodes. *Ceram. Int.* **2020**, *46* (4), 5323−5330.

(58) Wang, X.; Lin, S.; Tong, H.; Huang, Y.; Tong, P.; Zhao, B.; Dai, J.; Liang, C.; Wang, H.; Zhu, X. Two-dimensional V4C3MXene as high performance electrode materials for supercapacitors. *Electrochim. Acta* **2019**, *307*, 414−421.

(59) Li, H.; Wang, X.; Li, H.; Lin, S.; Zhao, B.; Dai, J.; Song, W.; Zhu, X.; Sun, Y. Capacitance improvements of V4C3Tx by NH3 annealing. *J. Alloys Compd.* **2019**, *784*, 923−930.

(60) Wang, X.; Li, H.; Li, H.; Lin, S.; Bai, J.; Dai, J.; Liang, C.; Zhu, X.; Sun, Y.; Dou, S. Heterostructures of Ni−Co−Al layered double hydroxide assembled on V 4 C 3 MXene for high-energy hybrid supercapacitors. *Journal of Materials Chemistry A* **2019**, *7* (5), 2291−2300.

(61) Syamsai, R.; Grace, A. N. Ta4C3MXene as supercapacitor electrodes. *J. Alloys Compd.* **2019**, *792*, 1230−1238.

(62) Garg, R.; Agarwal, A.; Agarwal, M. Synthesis and optimization of MXene for supercapacitor application. *Journal of Materials Science: Materials in Electronics* **2020**, *31*, 18614−18626.

(63) Garg, R.; Agarwal, A.; Agarwal, M. Effect of vanadium doping on MXene-based supercapacitor. *Journal of Materials Science: Materials in Electronics* **2021**, *32*, 22046−22059.

(64) Zahra, S. A.; Anasori, B.; Iqbal, M. Z.; Ravaux, F.; Al Tarawneh, M.; Rizwan, S. Enhanced electrochemical performance of vanadium carbide MXene composites for supercapacitors. *APL Materials* **2022**, *10* (6), No. 060901.

(65) He, H.; Xia, Q.; Wang, B.; Wang, L.; Hu, Q.; Zhou, A. Two-dimensional vanadium carbide (V2CTx) MXene as supercapacitor electrode in seawater electrolyte. *Chin. Chem. Lett.* **2020**, *31* (4), 984−987.

(66) Xie, J.; Yang, P.; Wang, Y.; Qi, T.; Lei, Y.; Li, C. M. Puzzles and confusions in supercapacitor and battery: Theory and solutions. *J. Power Sources* **2018**, *401*, 213−223.

(67) Mahmood, M.; Rasheed, A.; Ayman, I.; Rasheed, T.; Munir, S.; Ajmal, S.; Agboola, P. O.; Warsi, M. F.; Shahid, M. Synthesis of ultrathin MnO2 nanowire-intercalated 2D-MXenes for high-performance hybrid supercapacitors. *Energy Fuels* **2021**, *35* (4), 3469−3478.

(68) Mustafa, B.; Lu, W.; Wang, Z.; Lian, F.; Shen, A.; Yang, B.; Yuan, J.; Wu, C.; Liu, Y.; Hu, W.; Wang, L. Ultrahigh Energy and Power Densities of d-MXene-Based Symmetric Supercapacitors. *Nanomaterials* **2022**, *12* (19), 3294.

(69) Qiu, Z.; Wang, Y.; Bai, Y.; Zhang, S.; Lu, Z.; Sun, Y.; Xiong, T.; Xu, L.; Du, K.; Luo, Y.; Liu, G. Constructing KCu7S4/titanium carbide MXene hybrid structure via electrostatic assembly for high-performance supercapacitors. *J. Mater. Res.* **2023**, *38* (6), 1683−1693.

(70) Sharma, A.; Patra, A.; Namsheer, K.; Mane, P.; Chakraborty, B.; Rout, C. S. All-solid-state asymmetric supercapacitors based on VS 4 nano-bundles and MXene nanosheets. *J. Mater. Sci.* **2021**, *56*, 20008−20025.

(71) Alam, S.; Iqbal, M. Z. Nickel-manganese phosphate: An efficient battery-grade electrode for supercapattery devices. *Ceram. Int.* **2021**, *47* (8), 11220−11230.

(72) Alam, S.; Fiaz, F.; Khan, M. I.; Iqbal, M. Z.; Hegazy, H. H. Recent advancements in the performance of MXene and its various

composites as an electrode material in asymmetric supercapacitors. *J. Alloys Compd.* **2023**, No. 171007.

(73) Al-Kharafi, F.; Badawy, W. Electrochemical behaviour of vanadium in aqueous solutions of different pH. *Electrochimica acta* **1997**, *42* (4), 579−586.

(74) Mathis, T. S.; Kurra, N.; Wang, X.; Pinto, D.; Simon, P.; Gogotsi, Y. Energy storage data reporting in perspective—guidelines for interpreting the performance of electrochemical energy storage systems. *Adv. Energy Mater.* **2019**, *9* (39), No. 1902007.